International Journal of Heat and Mass Transfer 195 (2022) 123172

Contents lists available at ScienceDirect

International Journal of Heat and Mass Transfer

journal homepage: www.elsevier.com/locate/hmt

Impact of inflow turbulence on large-eddy simulation of film cooling flows

C.D. Ellis*, H. Xia

NCCAT, Department of Aeronautical and Automotive Engineering, Loughborough University, Loughborough, UK

ARTICLE INFO

Article history:
Received 7 April 2022
Revised 31 May 2022
Accepted 17 June 2022
Available online 30 June 2022

ABSTRACT

The paper investigates the impact of industrially appropriate inflow turbulence on the turbulent state, mixing capability and surface coolant distribution of film cooling flow using LES. Near-wall and freestream turbulence, corresponding to turbulent boundary layers and stochastic turbulent fluctuations away from the wall, have been investigated. In our study, we set up three main test scenarios: no inflow turbulence, near-wall boundary layer turbulence and freestream turbulence. Our work shows that surface adiabatic cooling effectiveness differs significantly with and without inflow turbulence. It is also evident that freestream turbulence enhances the mixing ability of a cooling flow, providing an initial enhancement of surface cooling close to the hole but with reduced cooling effectiveness downstream. Turbulent length scales, turbulent heat flux and turbulent anisotropy are compared and illustrate the changes in cooling effectiveness as a result of the upstream turbulent behaviour. As a result, despite inflow turbulence being a complex subject and problem-dependent, the importance of introducing realistic turbulent inflow in LES of cooling flows is demonstrated.

1. Introduction

Inflow turbulence plays a vital role in the simulation of turbulent flows and is an essential component in obtaining accurate simulation data with high-fidelity tools such as Large-Eddy Simulations (LES) and Direct Numerical Simulations (DNS). In film cooling flows, commonly found in gas turbine combustor and turbine systems, the turbulent state of the hot gas directly impacts the cooling performance of the flow and understanding its importance is critical. The present work assesses the impact of turbulent inflow conditions on mixing performance and cooling ability of film cooling type flows, demonstrating the importance of upstream fluctuations in simulations. For our film cooling studies, inflow turbulence can be loosely classified into near-wall turbulence, describing turbulent boundary layers, and Free-Stream Turbulence (FST), which corresponds to fluctuations away from the wall. The former conditions are common within experimental tests, while the latter is well-featured in gas turbine environments such as combustors, where the interacting port flow introduces large turbulent fluctuations across the cooling holes in the combustor liner.

Film cooling describes a group of methods that provide cooling flow across the surface of components exposed to hot fluids. Such components require advanced cooling mechanisms to improve component lifetimes, reducing the impact of creep, oxidation and softening. One cooling strategy is to introduce coolant through cooling holes distributed across the surface, providing a coolant film across the hot component. Adiabatic Cooling Effectiveness (ACE), $\eta_{aw} = (\overline{T}_{aw} - T_\infty)/(T_c - T_\infty)$, is used to establish the cooling performance, where T_c and T_∞ are the cold and mainstream gas temperatures and $\overline{T}_{aw}$ is the mean adiabatic wall temperature.

A fixed inlet velocity profile, without turbulent fluctuations, was used by Acharya and Leedom [1] in LES studies of a singular cooling hole. ACE results close to the hole trailing edge showed good agreement with experiments, however, the downstream ACE was overpredicted. Furthermore, a strong horseshoe vortex was shown ahead of the coolant hole, entraining coolant upstream. Renze et al. [2] numerically investigated coolant jets at low blowing ratios using a compressible recycling-rescaling method to generate inflow boundary layer turbulence across the near-wall. Ahead of the cooling hole, hairpin-like structures are shown to interact with the shear layer between the coolant and mainstream flow. The approach provided a good agreement to experimental cooling results.

For Free-Stream Turbulence (FST) investigations, Mayhew et al. [3] experimentally demonstrated that at blowing ratios between 0.5 and 1.0 a FST intensity of 10% reduced the surface averaged ACE, but had little effect at higher blowing ratios ($BR = 1.5$). Kohli

* Corresponding author.
E-mail address: c.d.ellis@lboro.ac.uk (C.D. Ellis).

https://doi.org/10.1016/j.ijheatmasstransfer.2022.123172

Nomenclature

Roman Symbols

a_{ij}	Anisotropy Tensor
b_i	Dimensional Filter Coefficients
C_w	Model Constant
D	Coolant Hole Diameter (m)
E_{ij}	Velocity Spectra (m^2/s^2)
f_{ij}^k	Two-point Correlation Function
g_{ij}	Velocity Gradient Tensor $(1/s)$
h	Enthalpy (J/kg)
k	Turbulent Kinetic Energy (m^2/s^2)
l	Coolant Hole Length (m)
L	Turbulent/Integral Lengthscale (m)
L_{ij}^k	Integral Length Scale (m)
L_{ij}	Lower Triangular Matrix of the Cholesky Decomposisiton of R_{ij} (m/s)
p	Pitch (m) / Pressure (Pa)
q_i	Heat Flux Vector (m^3/s^3)
R_{ij}	Reynolds Stress Tensor (m^2/s^2)
S_{ij}	Strain-rate Tensor $(1/s)$
T	Temperature (K)
Tu	Turbulent Intensity
t^*	Convective Time (s)
u_i/U	Velocity (m/s)
v	Unscaled Velocity Field
x / X	X Coordinate (m)
y / Y	Y Coordinate (m)
z / Z	Z Coordinate (m)

Greek Symbols

α	Inclination Angle $(^\circ)$ / Diffusivity (m^2/s)
δ_{ij}	Identity Matrix
η_{aw}	Adiabatic Cooling Effectiveness
κ	Wave Number
μ	Dynamic Viscosity $(kg/m/s)$
ν	Kinematic Viscosity (m^2/s)
ρ	Density (kg/m^3)
τ	Stress Tensor (m^2/s^2)
ξ	Random Vector Field
ζ_{ij}	Symmetric Square of the Velocity Gradient Tensor $(1/s^2)$

Subscripts/Subscripts

$\overline{\square}$	Time-averaged Property
$\square_0$	Total Property
$\square_t$	Time Step
$\square_{aw}$	Adiabatic Wall Value
$\square_c$	Coolant Property
$\square_{rms}$	Root-Mean-Square
$\square_{sgs}$	Sub-grid Scale Property
$\square_\infty$	Freestream Property
$\tilde{\square}$	Favre-averaged Property
$\square'$	Fluctuating Property
$\square^*$	Traceless Property

Abbreviations

ACE	Adiabatic Cooling Effectiveness
BR	Blowing Ratio
DNS	Direct Numerical Simulation
FST	Free-Stream Turbulence
LES	Large Eddy Simulation
RANS	Reynolds-Averaged Navier-Stokes

and Bogard [4] conducted studies at a FST intensity of 20%, where the large scale turbulent structures from the mainstream flow superseded the turbulent structures generated by the shear layer of the coolant jet, elevating the mixing and reducing the cooling effectiveness. A hybrid LES-RANS approach is used by Chen and Xia [5] to study an effusion cooling array with FST generated with a synthetic coherent eddy method at a FST intensity of 5%. Kelvin-Helmholtz structures are observed in the shear layer of the first hole before breaking down into smaller, three-dimensional structures. Spanwise-averaged ACE is well-matched to the experiment after the final hole, but the development of the coolant is slower across the holes.

Busche et al. [6] investigated FST intensity from 0.7% to 13.7% on a slot cooling system and showed increasing FST intensity negatively affects the cooling ability of the system. The same case was studied with LES by Kanani et al. [7] for slot film cooling. Results showed a decrease in slot cooling effectiveness and an increase in heat transfer coefficient with increasing FST intensity. Schroeder and Thole [8] investigated the effect of FST intensities from 0.5% to 13% on shaped film cooling holes. The results showed the FST had a minimal effect on the mean velocity field but increased the turbulent intensity around the jet and lateral spreading of coolant.

A single-row film cooling geometry, experimentally investigated by Sinha et al. [9] and Pietrzyk et al. [10], is studied in this paper. Three diverse cases of different inflow conditions are compared to illustrate the impact on mixing behaviour and cooling performance of the flow across these conditions, providing a good reference for future film cooling studies. This study adds to the current literature by comparing a case with no inflow turbulence with a case with near-wall turbulence to highlight the importance of the near-wall turbulence in experimental configurations. A high freestream turbulence case is pursued to provide a case with industrial focus where cooling flows are exposed to large turbulent intensities.

The results of the paper highlight differences in time-averaged ACE, the mixing capability and the turbulent state of the flows across these distinctly different cases. Turbulent anisotropy, heat flux and length scales are used to assess the mixing capabilities of the flows. Correct inflow turbulent conditions in LES simulations for near-wall turbulent flow is shown to be crucial to accurately predict the complex mixing behaviours of coolant flow.

2. Numerical details

2.1. Geometry

The single-row film cooling geometry studied features a cylindrical hole with a diameter of 12.7 mm and an inclination angle, α, of 35°. The coolant holes are short, with a length-to-diameter ratio, l/D, of 1.75, and laterally distributed with a pitch-to-diameter ratio, p/D, of 3. Parameters are illustrated in Fig. 1. The simulation is performed at a blowing ratio of 1.0 and density ratio of 2.0, as studied by Sinha et al. [9]. Under these conditions, the momentum of the coolant jet is large enough to provide jet lift-off and thus the mainstream-coolant interaction is a critical mechanism driving surface temperatures.

2.2. Governing equations and solver

LES simulations are performed using OpenFOAM v1712 [11] and its *rhoPimpleFoam* finite volume solver. The pressure-based solver is used for transient simulations of turbulent flow. For the present simulations, the solver is run using the Pressure Implicit Split Operator (PISO) mode for coupling the continuity and momentum equations. Conservation equations for continuity, momentum and energy are solved with the following forms respectively:

$$\frac{\partial \bar{\rho}}{\partial t} + \frac{\partial \bar{\rho}\tilde{u}_i}{\partial x_i} = 0, \tag{1}$$

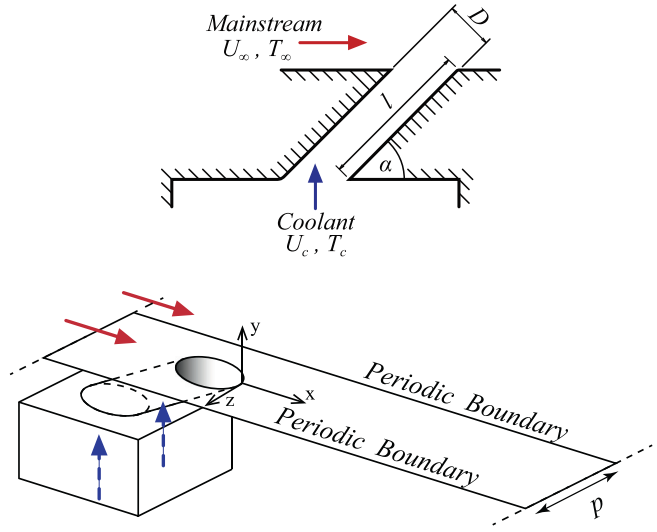

Fig. 1. Coolant hole domain parameters.

$$\frac{\partial \bar{\rho}\tilde{u}_i}{\partial t} + \frac{\partial \bar{\rho}\tilde{u}_i\tilde{u}_j}{\partial x_j} = -\frac{\partial \bar{p}}{\partial x_i} + \frac{\partial}{\partial x_j}\left(2\mu\tilde{S}^*_{ij} - \bar{\rho}\tau^{sgs}_{ij}\right), \tag{2}$$

$$\frac{\partial \bar{\rho}\tilde{h}_0}{\partial t} + \frac{\partial \bar{\rho}\tilde{u}_j\tilde{h}_0}{\partial x_j} = \frac{\partial}{\partial x_j}\left(\bar{\rho}\alpha\frac{\partial \tilde{h}}{\partial x_j} - \bar{\rho}q^{sgs}_j\right), \tag{3}$$

where,

$$\tau_{ij} = -2\nu_{sgs}\tilde{S}^*_{ij}, \tag{4}$$

and,

$$\tilde{S}^*_{ij} = \frac{1}{2}\left(\frac{\partial \tilde{u}_i}{\partial x_j} + \frac{\partial \tilde{u}_j}{\partial x_i}\right) - \frac{1}{3}\frac{\partial \tilde{u}_k}{\partial x_k}. \tag{5}$$

In the above equations, sub-grid scale stresses, τ^{sgs}_{ij}, are modelled with the Wall-Adaptive Local Eddy-viscosity (WALE) of Nicoud and Ducros [12], where the tensor is described by the modelled sub-grid scale viscosity, ν_{sgs}, and the mesh resolved traceless strain rate tensor, $\tilde{S}^*_{ij}$. Correct y^3 near-wall scaling of the sub-grid scale viscosity is achieved with the WALE model without the need for dynamic formulations. WALE has been successfully used within conjugate heat transfer simulations of cooled turbine blades [13], the flow and heat transfer of two cylinders in tandem [14] and rib-roughened internal turbine blade cooling channels [15]. The sub-grid scale viscosity is obtained from Eq. (6) where the cube root of the cell's volume is used for the filtered length scale, Δ, and the model coefficient, C_w, of 0.325 is used. The definition of ζ^*_{ij} is shown in Eq. (7) forming the traceless symmetric component of the square of the velocity gradient tensor, $\bar{g}_{ij}$.

$$\nu_{sgs} = (C_w\Delta)^2\frac{(\zeta^*_{ij}\zeta^*_{ij})^{3/2}}{(\bar{S}_{ij}\bar{S}_{ij})^{5/2} + (\zeta^*_{ij}\zeta^*_{ij})^{5/4}} \tag{6}$$

$$\zeta^d_{ij} = \frac{1}{2}\left(\bar{g}^2_{ij} + \bar{g}^2_{ji}\right)) - \frac{1}{3}\delta_{ij}\bar{g}^2_{kk} \tag{7}$$

$$\bar{g}_{ij} = \frac{\partial \bar{u}_i}{\partial x_j} \tag{8}$$

Sub-grid scale contributions to thermal diffusivity are achieved with a sub-grid scale Prandtl number of 0.4, providing successful results in Schindler et al. [16] and Ellis and Xia [17]. Contributions to the energy equations are shown by Eq. (9) where the sub-grid scale turbulent diffusivity is defined by Eq. (10).

$$q_{j,sgs} = -\alpha_{sgs}\frac{\partial h}{\partial x_j} \tag{9}$$

$$\alpha_{sgs} = \frac{\nu_{sgs}}{Pr_{sgs}} \tag{10}$$

In the present study, numerical schemes are selected to achieve the highest accuracy without compromising the numerical stability of the finite volume solver. A second-order blended scheme is used for the convective terms. A pure second-order scheme is blended with a second-order upwinding scheme where the factor controlling the blending is set to use 80% of the pure second-order scheme within and close to the jet and the wall with a smooth decrease to a value of 20% towards the far-field flow and outlet. This benefits the simulation by providing more of the numerically stable second-order upwinding scheme in regions away from the coolant jet with the accuracy of the pure second-order scheme resolving the turbulent fluctuations. A first-order Euler scheme is used for the temporal discretisation to ensure the numerical stability of the simulation while a very small time step provides high temporal resolution. The selected time step provides a ratio of $t^*/\Delta t$ of 1270, where the convective time step is defined as $t^* = D/U_\infty$. The maximum CFL in the simulation from the selected time-step is 0.7. The statistical data presented in this work has been obtained over a period of $625t^*$.

2.3. Mesh and domain

A mesh with hexahedral elements (Fig. 2) is generated across the domain. Near-wall cells are sized to achieve a maximum $\overline{\Delta y^+}$ of 1 across the coolant plate in the near-wall inflow turbulence case and streamwise and spanwise cell sizes obtain a $\overline{\Delta x^+} < 26$ and $\overline{\Delta z^+} < 11$ in the upstream boundary layer flow. Aft of the hole trailing edge a cell size of $\overline{\Delta x^+} < 23$ and $\overline{\Delta z^+} < 23$ is obtained. The resulting mesh size is 20.6 million cells. The sensitivity of the mesh resolution was assessed in a preliminary investigation before the upstream turbulent inflow and velocity profile were finalised for the present study. The 80 million cell mesh added further refinement in all spatial directions. The finer mesh and its solution showed negligible differences in surface ACE when compared to the results of the 20.6 million cell case.

The resolved-to-total ratio of turbulent kinetic energy, r_k (Eq. (11)) also known as Pope's criterion, is shown across streamwise planes in Fig. 3. For much of the simulated domain, the high mesh-resolution achieves values of r_k greater than 0.96, with the lowest values of 0.9 seen at the edge of the coolant hole, where the coolant hole intersects the coolant plate.

$$r_k = \frac{k_{res}}{\bar{k}_{sgs} + k_{res}} \tag{11}$$

The computational domain is set up across a single hole with periodic boundaries at the spanwise planes (Fig. 1) to simulate the row of holes. A fixed pressure outlet is used far downstream and a freestream boundary condition is applied to the top of the domain. No-slip adiabatic walls are applied across the plate, coolant hole, and the top of the coolant plenum. Coolant is supplied via the coolant plenum, where a constant mass flow is supplied to achieve the required blowing ratio. Upstream of the coolant hole, the inlet boundary condition supplies a turbulent hot mainstream flow. Inflow turbulence is generated at the inlet using a modification of Klein et al. [18] digital-filtered technique published by Immer [19].

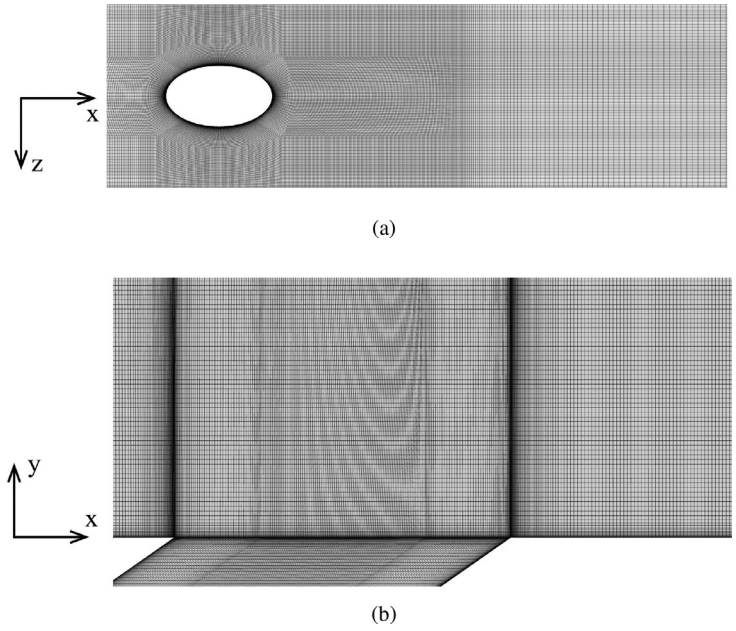

Fig. 2. Hexahedral mesh showing (a) the plate surface mesh and (b) the centre plane cross-section of the mesh.

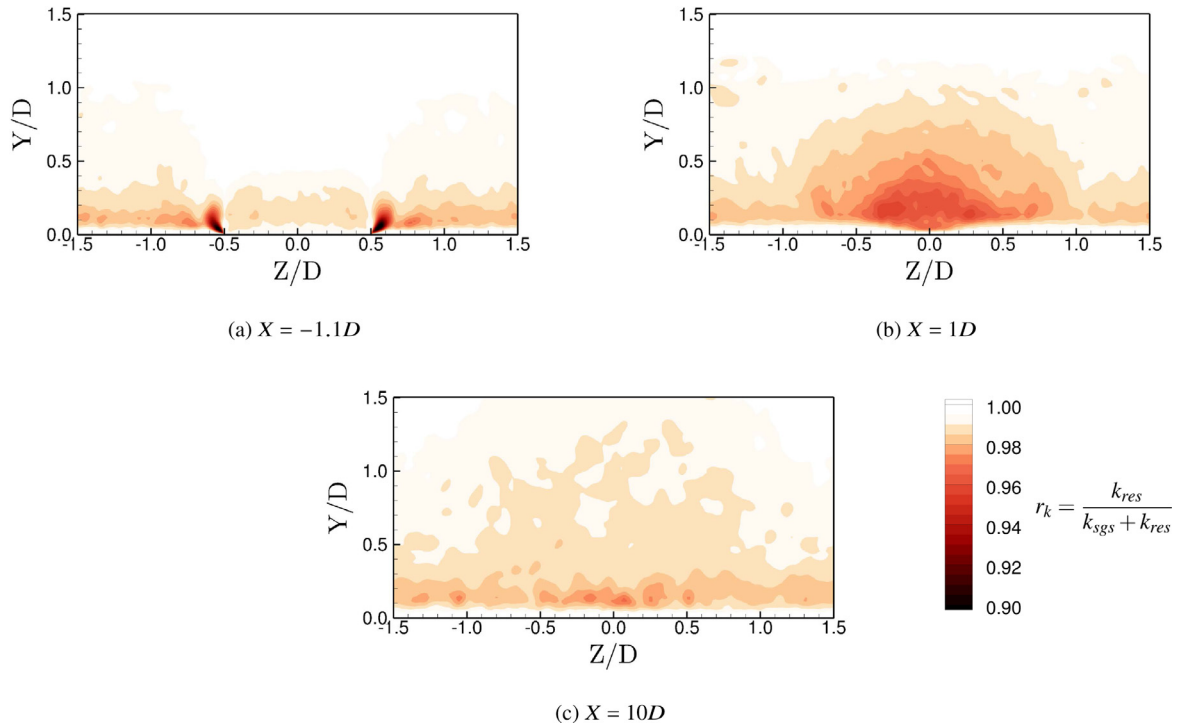

Fig. 3. Contours showing the ratio of resolved to total turbulent kinetic energy at three streamwise planes for `01NWL1`.

Digital filtering techniques provide an efficient method for correlated turbulent fluctuations.

2.4. Digital filtering turbulence

Many different methods exist to supply turbulence at the inlet boundary condition. White noise methods apply a random velocity perturbation that yields the desired first and second-order statistics at the inlet but fails to establish the classic energy cascade and the correct length and time scales of the turbulent fluctuations. Precursor simulations provide a physical description of turbulence with turbulent statistics and coherence providing the mesh is sufficiently fine, but these methods are computationally expensive. Synthetic eddy methods mimic the structure of the eddies that are then randomly distributed across a virtual box and convected through the inlet boundary to simulate turbulent spots. Digital filtering techniques aim to spatially and temporally correlate a random noise field at the inlet. Such a method is attractive

because of its ability to create realistic turbulence for small inlet grids.

The digital filtering method takes a random vector field, ξ_i, with a normal distribution generated across a virtual cartesian grid. The virtual grid is imposed over the unstructured inlet mesh. Two-dimensional spatial filtering of the random vector field is performed for each component of ξ_i, across the two dimensions of the cartesian grid:

$$\upsilon_{m,n} = \sum_{j=-N_y}^{N_y} \sum_{k=-N_z}^{N_z} b_{j,k} \xi_{m+j,n+k}, \tag{12}$$

where the two-dimensional filter coefficients are:

$$b_{j,k} = b_j * b_k. \tag{13}$$

For the present study, a Gaussian filter is used, establishing the filter coefficients as:

$$b_j = \frac{e^{-\pi j^2/2L^2}}{\tilde{b}}, \tag{14}$$

where L is the specified integral length scale and,

$$\tilde{b} = \sqrt{\sum_{i=0}^{N} b_i^2}. \tag{15}$$

The correlation in the third spatial dimension is performed in the temporal domain with an Autoregressive model, where Δt and I_t are the simulation timestep and integral time scale. The unscaled velocity field, v_t, is calculated in Eq. (16) with the previous timestep's field and the current random filtered velocity field, υ_t, determined from Eq. (12).

$$v_t = v_{t-1} e^{-\Delta t/I_t} + \upsilon_t \sqrt{1 - e^{-2\Delta t/I_t}} \tag{16}$$

Finally, the correlation between the components of the filtered vector field v_i is sought to achieve the prescribed Reynolds stresses from the fluctuating velocities, u_i. The correlation provides the fluctuating velocities from the following transformation:

$$u_i = L_{i,j} v_i, \tag{17}$$

where $L_{i,j}$ is the lower triangular matrix of the Cholesky decomposition of the prescribed Reynolds stress tensor, shown to be:

$$L_{ij} = \begin{bmatrix} \sqrt{R_{11}} & 0 & 0 \\ \frac{R_{12}}{L_{11}} & \sqrt{R_{22} - L_{21}^2} & 0 \\ \frac{R_{13}}{L_{11}} & \frac{R_{23} - L_{21}L_{31}}{L_{22}} & \sqrt{R_{33} - L_{31}^2 - L_{32}^2} \end{bmatrix}. \tag{18}$$

Table 1
Table of cases and inflow turbulent information.

Case Name	Inflow Turbulence State	Tu	L
NoTurb	No Fluctuations	-	-
01NWL1	Near-wall Developing Turbulent Boundary Layer	0.1%	1D
20FSTL1	High Freestream Turbulence	20%	1D

The fluctuating velocities are then computed at every timestep and added to the prescribed mean velocities, obtaining correlated inflow turbulent fluctuations to user-specified profiles.

Three inlet condition scenarios are investigated: NoTurb, 01NWL1 and 20FSTL1. A summary of the conditions are provided in Table 1. First, NoTurb (Fig. 4a) is a fixed velocity profile without turbulent velocity fluctuations. Second, 01NWL1 (Fig. 4b) uses measured velocity and Reynolds stress profiles, that replicate the turbulent near-wall fluctuations associated with the turbulent flow upstream of the wind tunnel. Finally, 20FSTL1 (Fig. 4c) demonstrates the elevated fluctuations akin to a gas turbine environment, with a FST intensity of 20%. At the inflow boundary, a turbulent length scale of 1D is specified away from the wall. Although the length scales in gas turbine flows surpass the size of the intricate coolant holes, the specified length scale accounts for the smaller scales closer to the walls in wall-bounded flows. Towards the wall, the specified length scale reduces to a value of 0 at the wall and provides a length scale to local wall distance ratio of 2.5 in the near-wall region [20]. Experimental velocity and Reynolds stress profiles are taken from Pietrzyk et al. [10] preceding the work of Sinha et al. [9]. To provide an adequate development length between the inflow boundary and the cooling hole required for the digital filtering technique, the inflow boundary is placed 7D upstream of the coolant hole leading edge.

To demonstrate that the digital filtering method provides realistic turbulence and that the distance between the coolant hole and the inlet boundary is sufficient for synthetic turbulence development, Fig. 5 compares case 01NWL1 profiles to the experimental profiles [10] 1D upstream of the coolant hole. The streamwise velocity profile shows the LES captures the developing turbulent boundary layer well. Streamwise, normal, spanwise and shear turbulent stresses show close agreement with the experiment. However, the near-wall region exhibits a small increase in $\overline{u'u'}$ while other profiles show a closer agreement with the experimental measurements. For comparison, the streamwise velocity profile is shown for case NoTurb where when only the experimental veloc-

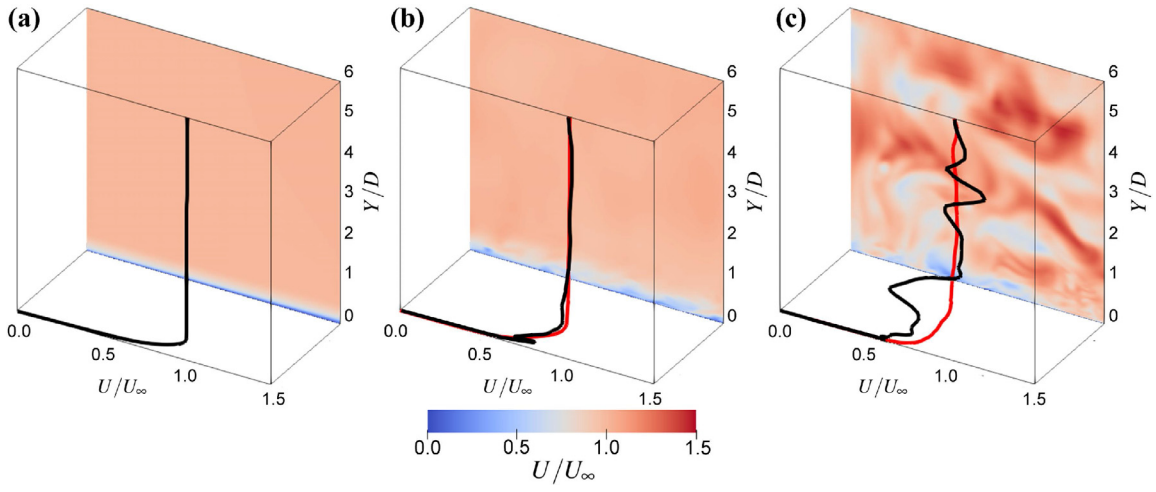

Fig. 4. Inflow turbulence conditions: (a) NoTurb, (b) 01NWL1 and (c) 20FSTL1.

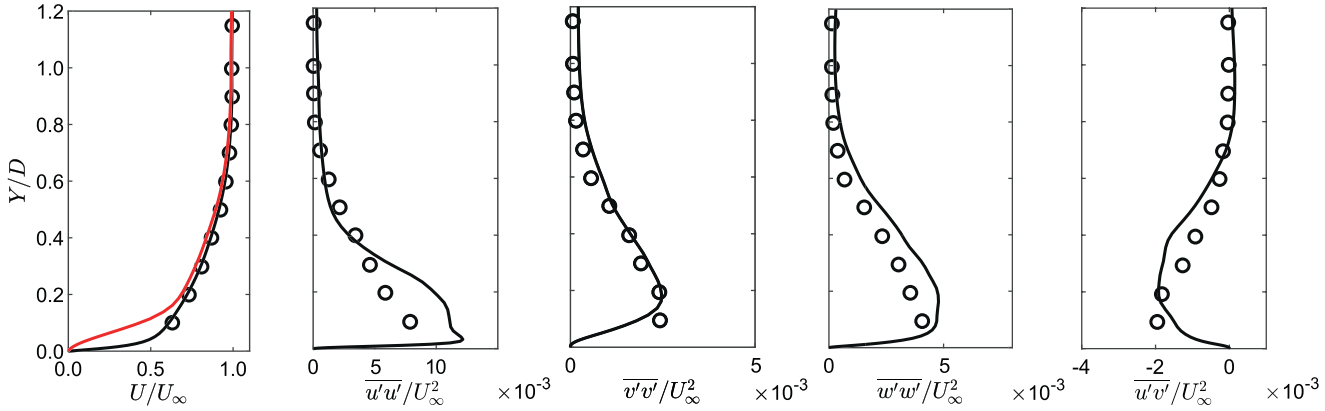

Fig. 5. Profiles downstream of inlet illustrating the behaviour of turbulent fluctuations introduced using the digital filtering turbulent inlet. `NoTurb` [——], `01NWL1` [——] and Pietrzyk et al. [10] [○].

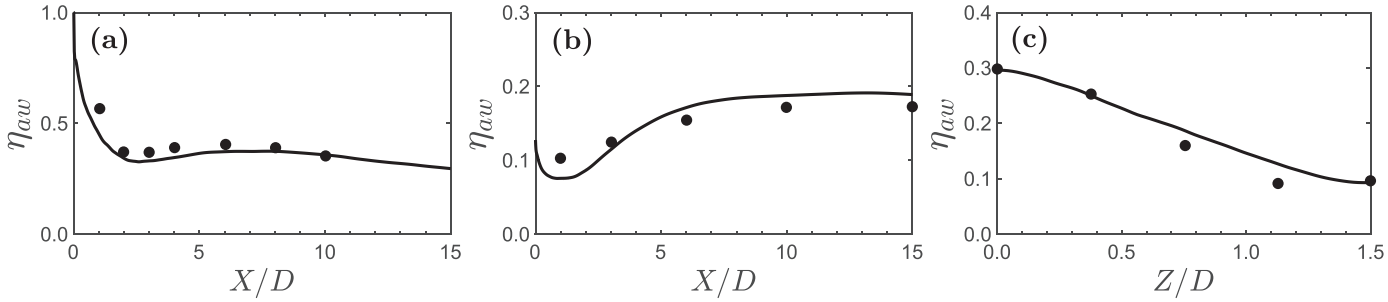

Fig. 6. ACE comparisons of `01NWL1` [——] with comparisons to experimental measurements of Sinha et al. [9] [●]. (a) Centreline, (b) Laterally-averaged and (c) Lateral $x = 15D$.

ity profile is provided to the mainstream inlet boundary condition and turbulent fluctuations are neglected.

3. Results and discussions

3.1. Cooling effectiveness

ACE is an effective indicator of well-captured dynamics and mixing in film cooling flows. Figure 6 presents results for case `01NWL1`, replicating the turbulent boundary layer of the experiment, where a good agreement to the published data of Sinha et al. [9] is found. Across the centreline (Fig. 6a), the numerical approach correctly captures the primary decline in coolant distribution and the local peak at $x = 6D$, associated with the jet reattachment which is not accurately captured in previous studies [1]. Good centreline effectiveness is presented in the work of Renze et al. [2], where the near-wall fluctuations are provided upstream. Lateral coolant spread is also well-captured by case `01NWL1`, shown in Fig. 6b and c, which is shown to be difficult to capture in numerical studies [1].

To illustrate the impact of the distinct cases of inflow turbulence Fig. 7 presents the time-averaged surface ACE showing the coolant distribution across the surface. For `NoTurb` and `01NWL1`, the surface coolant distribution can be described by a primary initial spreading of coolant from the trailing edge of the coolant hole followed by an increased lateral spreading from $1.5D$ downstream. `NoTurb` (Fig. 7a), shows minimal downstream lateral spread, whereas the addition of near-wall turbulent fluctuations in `01NWL1` (Fig. 7d) provides an increase in lateral spread. In comparison, the enhanced freestream turbulence of `20FSTL1` (Fig. 7g), does not exhibit the same trends as `NoTurb` and `01NWL1` but features greater lateral spreading immediately aft of the coolant hole, driven by the increased mixing ability of the flow. This trend replicates the results of the coolant slot flow in Busche et al. [6]. Upstream of the coolant hole, Fig. 7a shows that the absence of inflow turbulence provides upstream entrainment of coolant, arising from the horseshoe vortex as present in the contours shown by Acharya et al. [1].

Streamwise slices reveal the counter-rotating vortices that are well documented within these flows. The strength of these vortices, shown in Fig. 7c, f and i, decreases with the additional inflow turbulence. The local peaks of vorticity define the iconic kidney-bean shape of the counter-rotating vortices present in the non-dimensional temperature contour of cases `NoTurb` (Fig. 7b) and `01NWL1` (Fig. 7e). Comparing the non-dimensional temperature contour of `20FSTL1` shows a shift towards a circular-shaped contour of coolant. Additionally, the streamwise slices of non-dimensional temperature show the inflow turbulence of `01NWL1` (Fig. 7e) provide an increasing contribution to the vertical coolant spread and a further increase is evident in case `20FSTL1` (Fig. 7h).

Figure 8 shows quantitative time-averaged ACE distributions for the three inflow cases. Centreline results (Fig. 8a) show similar plots between `NoTurb` and `01NWL1`. The contrast between the two cases becomes apparent in the plots of lateral distribution (Fig. 8b and c). The addition of turbulent fluctuations in the upstream boundary layer promotes lateral spreading of coolant while maintaining a consistent centreline profile to `NoTurb`, shown in the contours of Fig. 7. With high FST, the trends of the ACE distribution shown in the preceding cases are no longer apparent. Centreline distributions (Fig. 8a) show a decaying trend with no downstream peak. This case provides an enhanced ACE distribution immediately aft of the hole trailing edge, shown in the laterally-averaged distribution (Fig. 8b) and the ACE map (Fig. 7g). Downstream distributions show a greater degree of lateral spread compared to the other cases, but a reduced ACE in the centreline, producing a near-uniform lateral distribution (Fig. 8c).

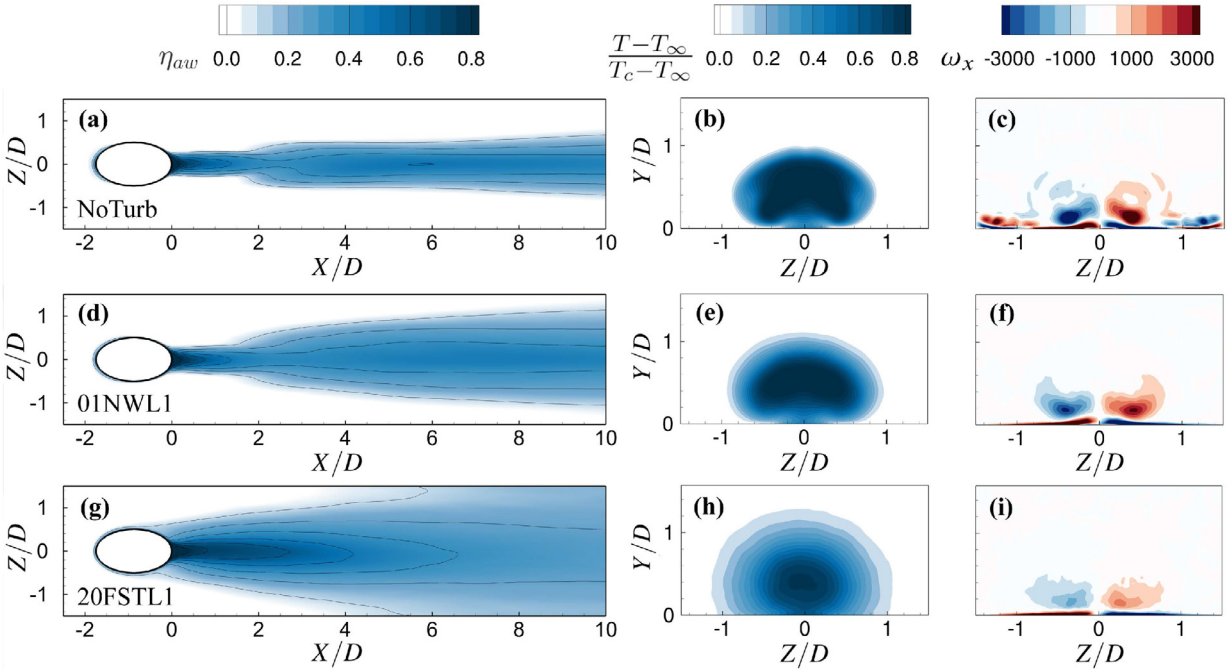

Fig. 7. ACE surface distributions, time-averaged non-dimensional temperature and streamwise vorticity ($x/D = 1.5$) comparing the three inflow conditions.

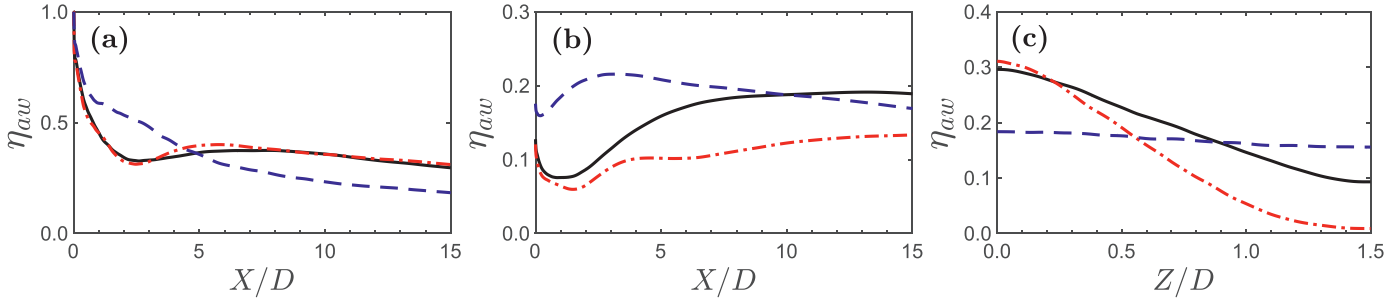

Fig. 8. ACE comparisons of `NoTurb` [-·-·-], `01NWL1` [——] and `20FSTL1` [- - -]. (a) Centreline, (b) Laterally-averaged and (c) Lateral $x = 15D$.

3.2. Flow structures

In the previous section, the time-averaged nature of the coolant distribution and comparisons between the three cases were formed. A detailed insight into the turbulent flow and its structures are sought in the present section to describe the change in cooling behaviours across the inflow turbulent conditions.

Figure 9 shows the comparisons of the instantaneous flow with isosurfaces of λ_2 criterion, showing highly vortical structures, and the instantaneous non-dimensional temperature across the centre plane. For `NoTurb` (Fig. 9a), the λ_2 criterion reveals a horseshoe vortex ahead of the coolant hole when no fluctuations are present in the inflow. The vortex wraps around the coolant stream providing a streamwise vorticity component away from the wall, shown in Fig. 7c. At $x = 3D$, these vortices are shown to break down into hairpin-like structures on both sides of the jet. The interaction between the mainstream and the coolant flow provides coherent, two-dimensional structures that form in the shear layer before breaking down at $x = 3D$, shown in Fig. 9a and b. These shear layer instabilities are also present in the effusion case of Chen and Xia [5], while Bogey et al. [21] discusses these linear instabilities forming in laminar jet flow.

Unlike `NoTurb`, the fluctuations of `01NWL1` (Fig. 9c) provide the near-wall three-dimensional hairpin-like structures that are present in turbulent boundary layer flow. These structures can qualitatively be seen to interact with the shear layer (Fig. 9d), destabilising the flow's ability to form coherent structures as shown in `NoTurb`. These structures are also present across the sides of the jet promoting lateral mixing from an earlier streamwise location. Case `20FSTL1` (Fig. 9e and f) highlights the extent at which the upstream turbulence interacts with the coolant jet. Comparing Fig. 9f with the other two cases, a qualitatively more chaotic field is seen. The large scale structures in the mainstream (Fig. 9e) dominate the flow and the turbulent structures generated within the shear layer as also discussed by Kohli and Bogard [4]. Small scale structures are visible in cases `NoTurb` and `01NWL1` (Fig. 9b and d), in the near-wall region downstream of the coolant hole trailing edge, whereas case `20FSTL1` shows qualitatively larger scales.

3.3. Reynolds stresses and anisotropy

Root-mean-square (RMS) velocity fluctuations and the turbulent shear stress $\overline{u'v'}$ are shown in Fig. 10 and compared for the three cases over a spanwise profile across the coolant jet. Close to the centreline, the RMS velocity fluctuations for `NoTurb` and `01NWL1` are similar. The differences are first shown in Fig. 10a where the inflow turbulence of `01NWL1` provides local maxima at the edge of the coolant jet. However, the greatest difference is exhibited in the fluctuations away from the jet centreline. All four figures show

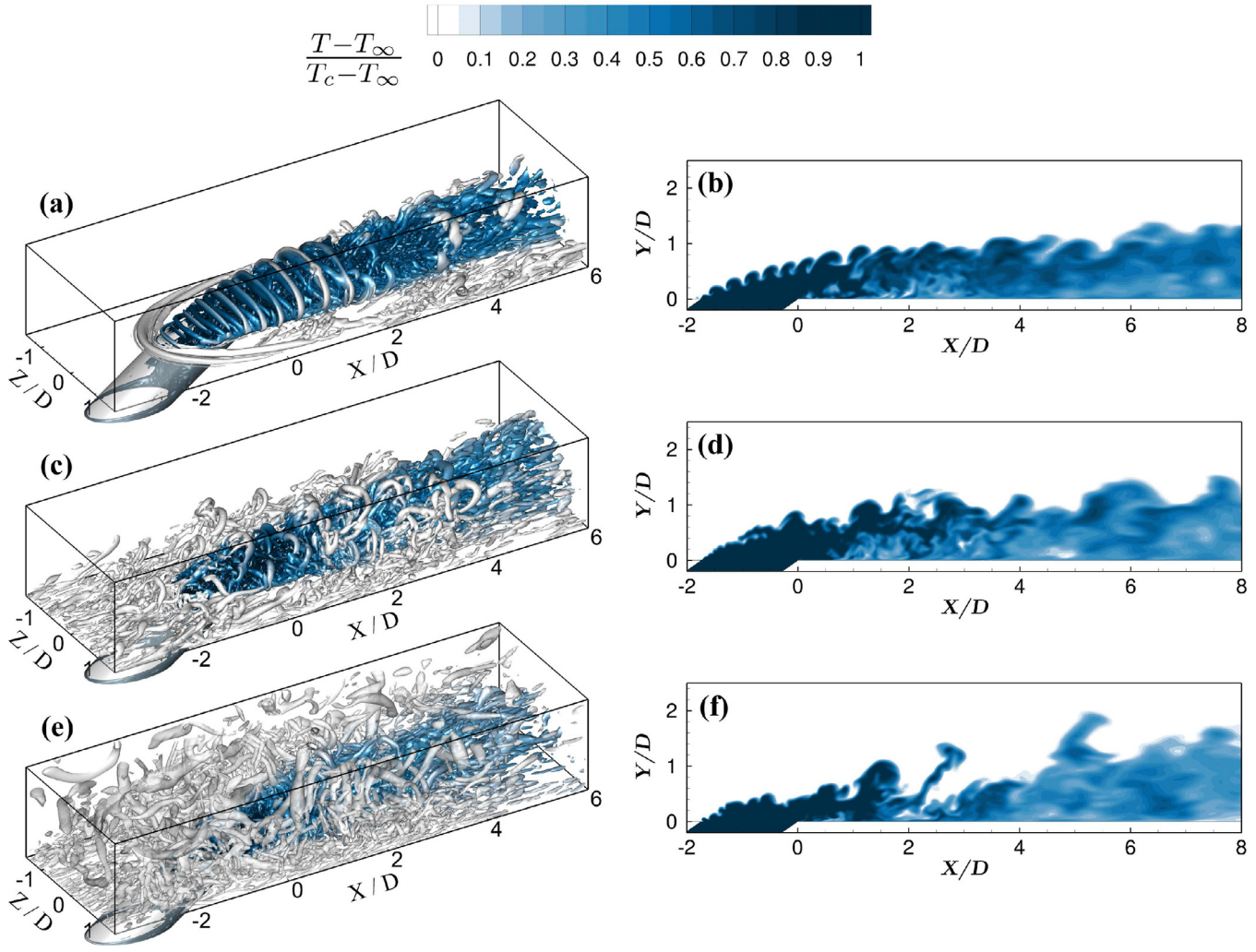

Fig. 9. Comparison of unsteady flow features using the λ_2 criterion (a, c, e) and normalised temperature (b, d, f) for (a-b) `NoTurb`, (c-d) `01NWL1` and (e-f) `20FSTL1`.

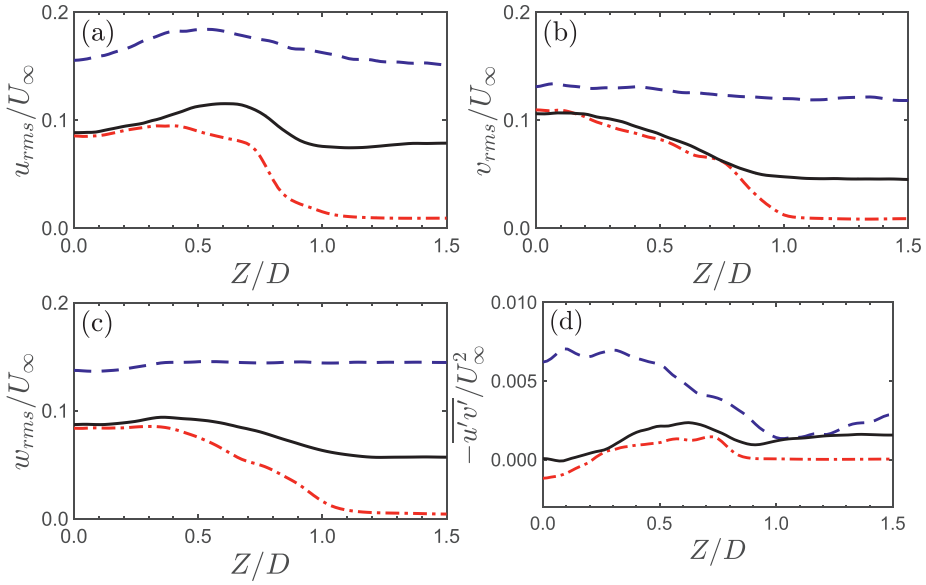

Fig. 10. Lateral comparisons of (a) u_{rms}/U_∞, (b) v_{rms}/U_∞, (c) w_{rms}/U_∞ and (d) $\overline{u'v'}/U_\infty^2$ at $x = 2.5D$, $y = 0.5D$. `NoTurb` [-·-], `01NWL1` [——] and `20FSTL1` [- - -].

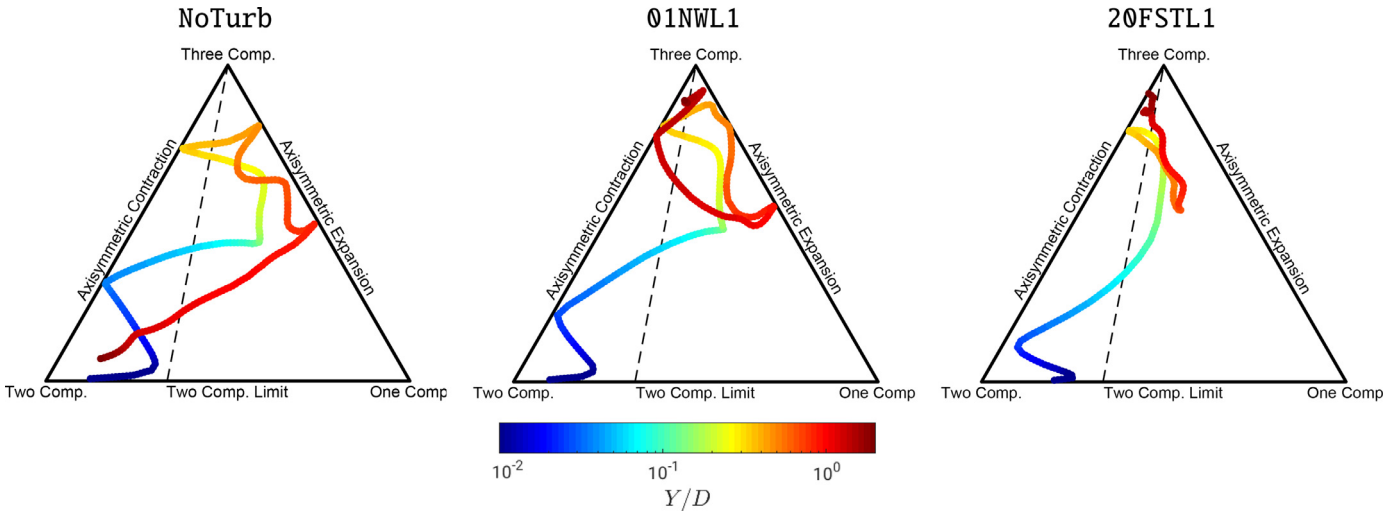

Fig. 11. Barycentric triangles of anisotropy comparing the anisotropic state of turbulence across the centreline profile at $x = 5D$. Plane-strain line [- - -].

this region has greater fluctuations for case 01NWL1 compared to the negligible fluctuations of case NoTurb. The greater magnitude of spanwise fluctuations in Fig. 10c, will provide increased lateral diffusion and provide the increased lateral spread shown in Figs. 7 and 8.

Case 20FSTL1 shows turbulent fluctuations that exceed those measured in 01NWL1 across the span profile. For w_{rms}, 20FSTL1 is up to 2.5 times greater than 01NWL1, facilitating an increased lateral coolant spreading ability. These increases are also shown in streamwise and normal components in Fig. 10a and b showing the elevated fluctuations that promote jet mixing. Figure 10d shows elevated turbulent shear stress within the jet core for the FST case; however, away from the jet centreline, the results show the correlation between streamwise and normal velocity fluctuations is comparable to case 01NWL1.

The anisotropy of the turbulence, described by Eq. (19), is a fundamental feature of the turbulence in both turbulent boundary layer and free-shear flows, influencing the turbulent transfer of the flows momentum and its mixing ability. Visualisation of the anisotropy and the anisotropic state of the flows is achieved using barycentric triangles of anisotropy. These triangles portray the realizable limits of the turbulent anisotropy bounded by the three corners and sides of the triangle. The three corners represent one-component, two-component and isotropic (three-component) turbulent states in the flow. Formation of the barycentric triangles is achieved by mapping the eigenvalues of the anisotropy tensor to the coordinates of the triangle and can be found in Banerjee et al. [22].

$$a_{ij} = \frac{\overline{u_i' u_j'}}{2k} - \frac{1}{3}\delta_{ij} \tag{19}$$

Figure 11 compares the anisotropy over the three cases across a profile on the jet-centreline downstream of the coolant hole trailing edge. All three cases exhibit similar near-wall behaviour with profiles ascending from the two-component limit state of turbulence to the axisymmetric contraction state. Diverging behaviours are then present in the remaining portion of the profile. First, case 20FSTL1 shows close alignment to the line of plain-strain turbulent behaviour, where the Reynolds stress components are proportional to the strain-rate components before increasing to near-isotropic turbulent behaviour.

Cases NoTurb and 01NWL1 show similar trends as the turbulence progresses towards the axisymmetric expansion state away from the near-wall region. This state signifies major fluctuations in a dominant direction and two minor, nearly equal fluctuating components in orthogonal directions to the major direction as would be expected in the outer layer of a turbulent boundary layer flow. The end of the profile at $y = 2D$, outside of the coolant jet, shows the deviation between cases NoTurb and 01NWL1, where the case without turbulence shows that the turbulent state progresses to the two-component corner, where the omission of three-dimensional fluctuations shows the flow is not turbulent in this outer boundary layer for case NoTurb. Case 01NWL1 at the end of the profile shows the turbulent state tends to an isotropic state in the freestream analogous to the behaviour of the high FST case.

Figure 12 provides comparisons across an off-centreline profile where large differences are seen in the Reynolds stresses shown in Fig. 10. Near-wall trends are similar between the three cases although the state of turbulence is closer to the two-component corner for the high FST case. Similar behaviours, close to the plane-strain line, are evident between cases 01NWL1 and 20FSTL1, although for some portion of the profile the 20FSTL1 case is closer to the axisymmetric contraction state. Away from the wall, case NoTurb shows turbulent behaviour that progresses towards axisymmetric expansion and back towards the non-turbulent, two-component corner of the triangle, diverging from the behaviour shown in cases 01NWL1 and 20FSTL1.

3.4. Turbulent heat flux

Quantifying the differing turbulent behaviour on the flow's mixing ability is sought by investigating the turbulent heat flux, $\overline{u_i' T'}$, across the three cases. The turbulent heat flux represents the local correlation of velocity and temperature fluctuations. Figure 13 compares the turbulent heat flux components across the three cases for a slice positioned $1D$ downstream of the cooling hole trailing edge.

The early stage of jet development, $1D$ downstream of the coolant hole trailing edge, shown in Fig. 13, portrays the initial coolant mixing behaviour across the three cases. The magnitudes of the turbulent heat flux vector components are shown to increase with the increasing turbulent intensity of each case. Component-wise, contrasting streamwise distributions are shown between the three cases, where negligible values are seen for the NoTurb case. The region of elevated turbulent heat flux components aligns with the shear layer for all three cases. Comparing case 01NWL1 to the high FST case 20FSTL1 shows the region of

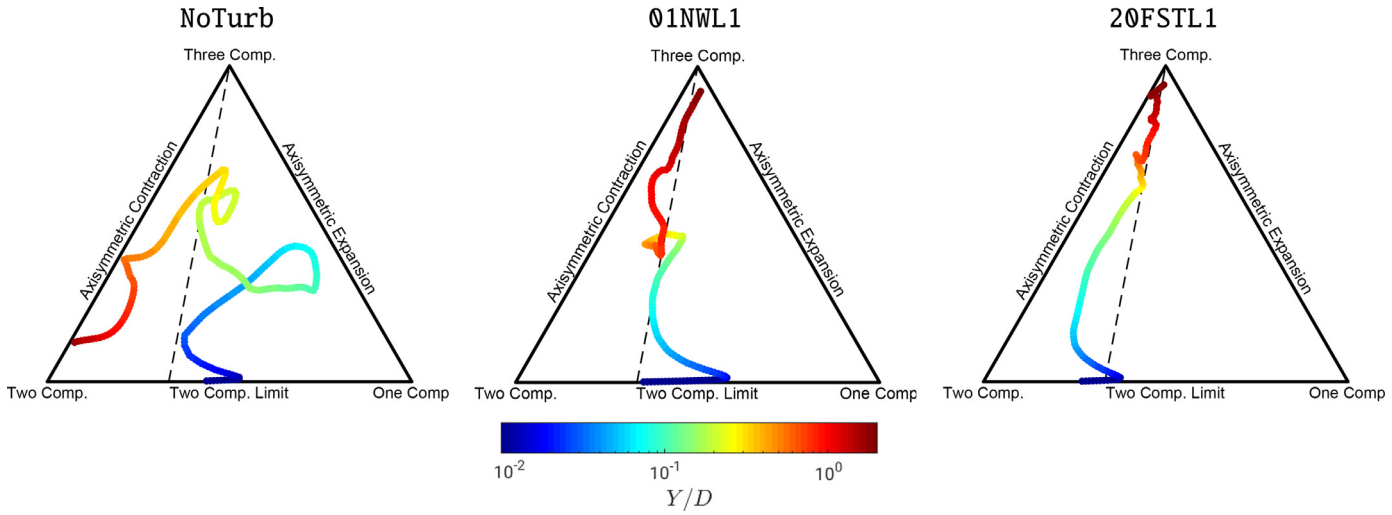

Fig. 12. Barycentric triangles of anisotropy comparing the anisotropic state of turbulence across the off-centreline profile at $x = 5D$, $z = 1D$. Plane-strain line [- - -].

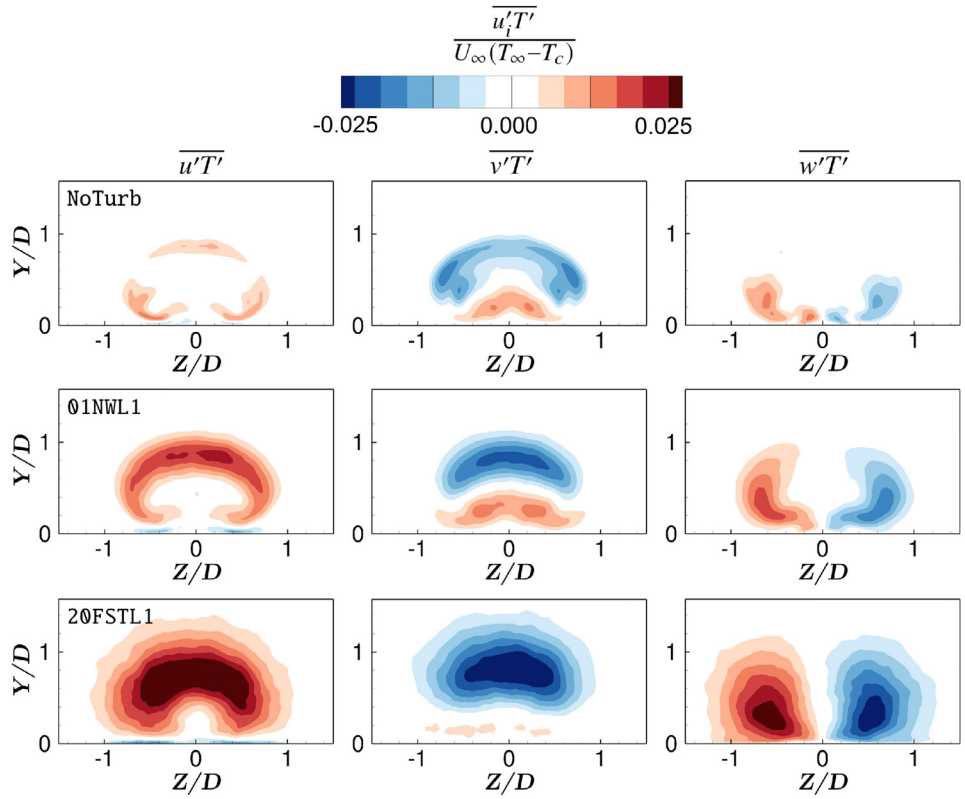

Fig. 13. Turbulent heat flux vector components compared across the three turbulent inflow cases at $1D$ downstream of the hole trailing edge.

high streamwise turbulent heat flux has an increased spread and intensity in case 20FSTL1, demonstrating its enhance mixing ability shown in ACE distributions of Figs. 8 and 7.

Spanwise components of turbulent heat flux, representing the correlation of spanwise fluctuating velocity with temperature fluctuations, show increasing magnitudes and spread of the parameter across the spanwise extent of the slice for the increasing intensities of each case. Comparisons between the spanwise turbulent heat flux and the cooling distribution contours shown in Fig. 7 show the locations of the elevated spread of coolant correspond to the elevated regions of turbulent heat flux in both the spanwise and normal components.

Figure 14 compares the centreline profiles of the streamwise and normal components of turbulent heat flux as the jet develops across the plate. The spanwise component is zero along planes of time-averaged symmetry. The largest contrast between the three cases is present at the $x = 0D$ and $x = 1D$ locations where the jet shear layer is in the early stages of development. At $x = 0D$, case 20FSTL1 shows the normal and streamwise components are of nearly equal, but opposite values across the profile, while case 01NWL1 shows a bias towards the normal component.

For case NoTurb, Fig. 14 shows a singular peak in the normal component of the turbulent flux at $x = 0D$. However, the streamwise component exhibits a double bump profile. The trend is a

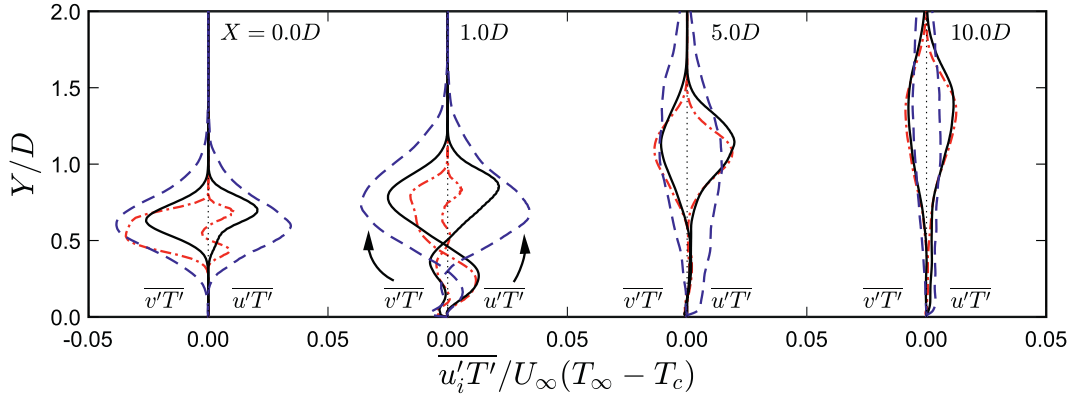

Fig. 14. Streamwise and normal turbulent heat flux ($\overline{u'T'}$ and $\overline{v'T'}$ respectively) development across profiles along the centreline. `NoTurb` [-·-], `01NWL1` [——] and `20FSTL1`[- - -].

feature of the shear layer instability, where vortices roll up in the shear layer. The fluctuations of the velocity parallel to the shear layer are present on either side of the shear layer, but in the location between the two peaks, the parallel velocity component is steady with negligible parallel velocity fluctuation. This behaviour is shown again at $x = 1D$. At $x = 5D$ the double peak behaviour is replaced by a singular peak, reflecting the turbulent transition that is also visible in the λ_2 isosurfaces of Fig. 9.

At $x = 1D$, the impact of the separated, rotating vortex flow from the trailing edge of the coolant hole provides a positive normal turbulent heat flux, shown below $y = 0.5D$. In this region, the magnitude of the normal turbulent heat flux is greater for cases `01NWL1` and `NoTurb` than case `20FSTL1`. This shows the high FST impacts the mixing of the immediately separated flow from the coolant hole trailing edge.

The greatest turbulent heat flux magnitude is exhibited by case `20FSTL1` at $x = 0D$ and $x = 1D$. Downstream, the shear layer peaks of streamwise turbulent heat flux for cases `NoTurb` and `01NWL1` are of similar magnitude and greater than that of case `20FSTL1`. However, the turbulent heat flux vector for case `20FSTL1` at $x = 5D$ shows the turbulent heat flux is spread and diffused across the profile, providing greater components of turbulent heat flux near the wall and into the freestream.

3.5. Length scales

A further quantitative assessment of coolant mixing can be made by assessing and comparing integral length scales across the coolant jet. Two-point correlations used to calculate the integral length scales, provide a value describing the correlation of a variable at one point in space to another variable at a second point in space. The streamwise integral length scale calculated from the two-point correlation function, Eq. (20). Similarly, the transverse length scales are calculated with Eq. (21).

$$L_{11}^{(1)}(\vec{x}) = \frac{1}{2}\int_{\vec{x}}^{\vec{x}+5D} f_{11}^{(1)}(x)\,dx \quad \text{where} \quad f_{11}^{(1)}(x) = \frac{\overline{u'(\vec{x}+x,t)u'(\vec{x},t)}}{\overline{u'(\vec{x},t)u'(\vec{x},t)}} \tag{20}$$

$$L_{33}^{(3)}(\vec{x}) = \frac{1}{2}\int_{-1.5D}^{1.5D} f_{33}^{(3)}(z)\,dz \quad \text{where} \quad f_{33}^{(3)}(z) = \frac{\overline{w'(\vec{x}+z,t)w'(\vec{x},t)}}{\overline{w'(\vec{x},t)w'(\vec{x},t)}} \tag{21}$$

Figure 15 shows the results of the two-point correlation function for the streamwise and spanwise length scale calculations at a location of $1D$ downstream of the cooling hole trailing edge at a height $0.1D$ above the coolant plate on the jet centreline. The

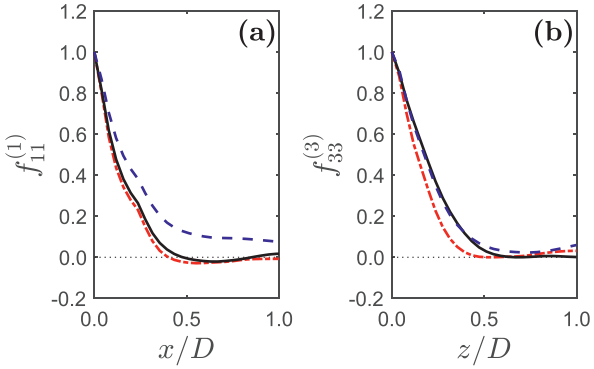

Fig. 15. (a) Streamwise and (b) spanwise two-point correlation function at $(1.0D, 0.1D, 0.0D)$. `NoTurb` [-·-], `01NWL1` [——] and `20FSTL1`[- - -].

two-point correlation, $f_{11}^{(1)}$, correlates the streamwise velocity fluctuation with itself in the streamwise direction, while $f_{33}^{(3)}$ shows the correlation of the spanwise velocity with itself in the spanwise direction. Results for Fig. 15a shows equivalent correlations between case `NoTurb` and `01NWL1`, indicating similar streamwise turbulent length scales at this location. For case `20FSTL1`, the correlation persists further downstream illustrating longer streamwise structures. The spanwise correlations in Fig. 15b, show similar correlations that reflect turbulent structures that have similar spanwise scales for all three conditions in this region of the flow.

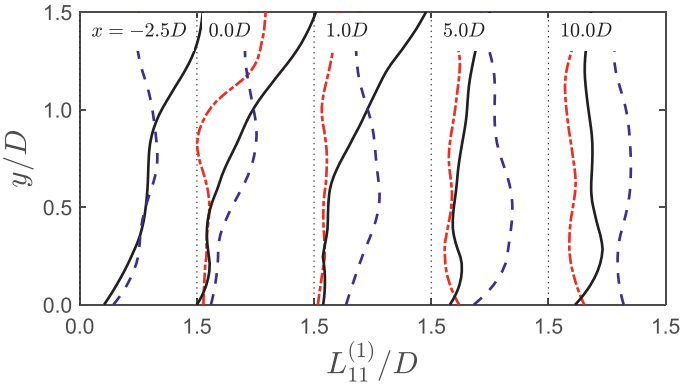

Fig. 16. Streamwise integral lengthscales, $L_{11}^{(1)}$, across centreline profiles. `NoTurb` [-·-], `01NWL1` [——] and `20FSTL1`[- - -].

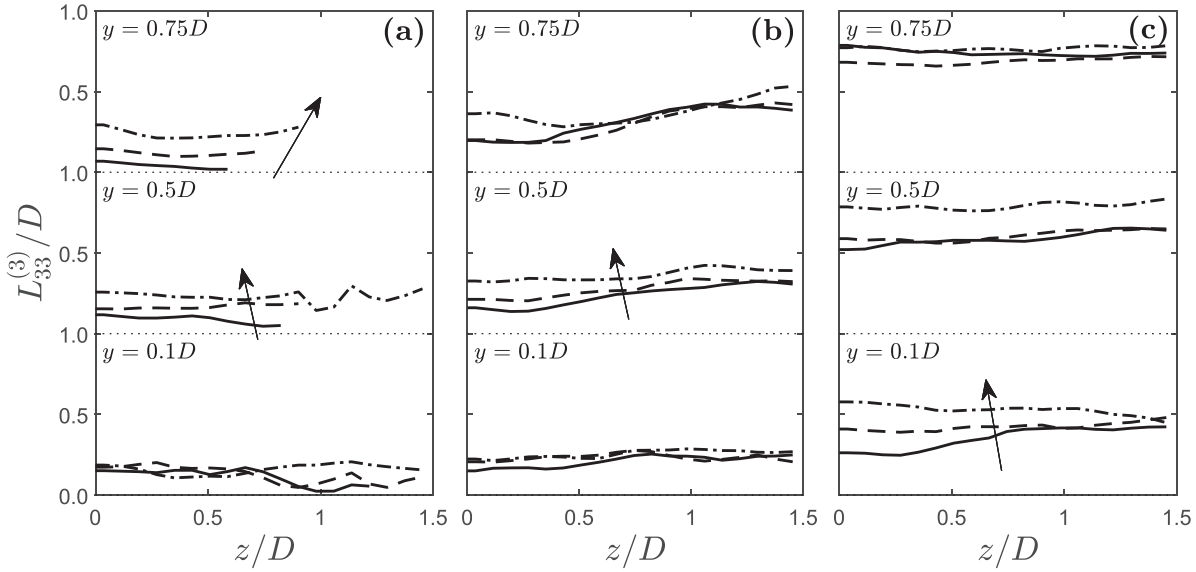

Fig. 17. Comparisons of transverse integral length scale, $L_{33}^{(3)}$, across transverse profiles for (a) NoTurb, (b) 01NWL1 and (c) 20FSTL1. Profiles located at $x = 1.0D$ [——], $x = 2.5D$ [- - -] and $x = 6.5D$ [-·-·-].

The length scales associated with the incoming boundary layers are shown in the first profile of Fig. 16 increasing from the wall to a size of $1D$. Away from the wall, $L_{11}^{(1)}$ becomes large for cases NoTurb and 01NWL1 where the fluctuating velocities approach zero. At the trailing edge of the hole (profile $x = 0.0D$), L_{11}^{1} shows smaller streamwise scales where the turbulent flow is driven by the separated flow within the coolant hole and aft of the sharp trailing. In this region, cases NoTurb and 01NWL1 show similar profiles demonstrating that the approaching turbulent boundary layer of 01NWL1 does not influence the scales of the structures within this region, while the larger fluctuations of case 20FSTL1 show greater scales. Figure 16 shows that these smaller length scales persist in the downstream profile of $x = 1.0D$ before an increase in $L_{11}^{(1)}$ is exhibited at $x = 5.0D$ for NoTurb and 01NWL1. The influence of the inflow near-wall fluctuations of 01NWL1 show a greater rate of $L_{11}^{(1)}$ growth, compared to NoTurb, as shown by the downstream profile at $x = 10.0D$. The growth of $L_{11}^{(1)}$ across the centreline is greater for 20FSTL1. At $x = 1.0D$ the length scales are equal to the length scales of $1D$ measured in the upstream flow and imposed at the inlet of the computational domain with the inflow turbulence generation.

Comparing the transverse integral length scales in Fig. 17 shows comparative trends to $L_{11}^{(1)}$. Blanking is performed for regions with very small fluctuations as shown by the scales away from the wall. Case NoTurb (Fig. 17a) demonstrates smaller scales when compared to the cases 01NWL1 (Fig. 17b) and 20FSTL1 (Fig. 17c), showing the introduction of upstream turbulence impacts the turbulent scales within the developing cooling jet. In profile $y = 0.1D$ of Fig. 17a, similar scales can be seen towards the jet centre, for all three streamwise profiles as the coolant jet interacts with the wall. At profiles away from the wall, the downstream progression of the coolant jet shows increasing values of $L_{33}^{(3)}$, demonstrating that within the coolant jet the length scales governing the turbulent mixing increase as the jet develops. This behaviour is most apparent for case NoTurb, but for cases 01NWL1 and 20FSTL1, this is only evident at positions closer to the wall.

Comparing cases NoTurb and 01NWL1, Fig. 17a and b respectively, the length scales remain similar downstream at $y = 0.1D$. At $y = 0.5D$ and $1.0D$ the length scales of 01NWL1 are greater than NoTurb showing at these positions in the jet, the impact of turbulence in the inflow boundary is critical to the mixing behaviour. The largest length scales of $L_{33}^{(3)}$ are shown in case 20FSTL1, where the length scales are shown to be near-uniform across the spanwise profiles apart from profiles near the wall at $X = 1.0D$.

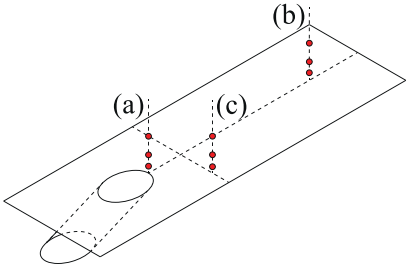

Fig. 18. Location of streamwise velocity spectra measurement points.

Further comparisons of the turbulent energy are made by investigating the streamwise velocity spectra, E_{11}, in Fig. 19. In the near-wall region at the trailing edge of the hole (Fig. 19a), all cases show similar spectra. This demonstrates that within this region, the impact of main flow inflow turbulence is negligible and the turbulent behaviour is driven by the separated region convected from the coolant hole, where the coolant inflow is constant across all cases. At $y = 0.5D$ and $1.0D$, 20FSTL1 shows a larger magnitude at low wavenumbers. At $y = 1.0D$, NoTurb provides a peak at $\kappa_1 = 29.9$, which is likely to be associated with the coherent vortex roll-up in the shear layer, shown by λ_2 surfaces in Fig. 9a. Figure 19b shows all cases align to the $-5/3$ slope, in the downstream region, highlighting the full three-dimensional behaviour of the turbulence associated with the inertial transfer of energy.

Figure 19 c, away from the jet centre shows contrasting behaviour between the cases. As expected, the higher energy fluctuations of 20FSTL1 provide greater magnitudes in the spectra. For NoTurb, the peak shown in Fig. 19a is also present at $y = 0.5D$ and $1.0D$. This highlights that the coherent structures shown in Fig. 9a are also providing a repeating behaviour along the sides of the jet rather than turbulent fluctuations that promote lateral mixing.

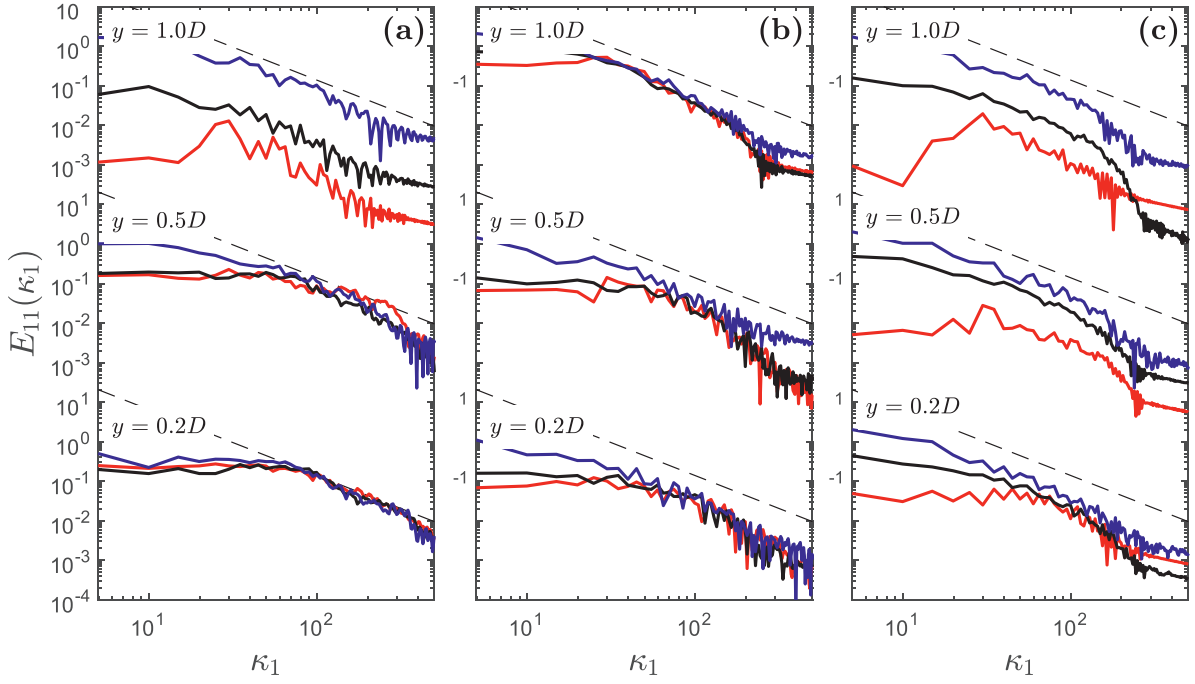

Fig. 19. Streamwise velocity spectra across jet development. (a) $x = 0D$ & $z = 0D$, (b) $x = 5D$ & $z = 0D$ and (c) $x = 1D$ & $z = 5D$, further shown in Fig. 18. `NoTurb` [——], `01NWL1` [——], `20FSTL1` [——] and $-5/3$ slope [- - -].

4. Conclusions

The work presented shows a well-motivated study of the impact of inflow turbulence on LES of film cooling flows. A well-documented cooling hole was chosen for our tests. Three different scenarios were investigated. First, `NoTurb`, with a mean velocity profile absent of turbulent inflow fluctuations. Then, `01NWL1`, with near-wall turbulent fluctuations reflecting the experimental turbulent boundary layer conditions, and finally, `20FSTL1` with 20% FST akin to combustor-like environments.

Centreline ACE profiles remain comprehensively similar between the case without inflow turbulence (`NoTurb`) and the case with only near-wall turbulence (`01NWL1`). However, case `01NWL1` provides turbulent fluctuations and coolant jet behaviour that reproduces the lateral spread demonstrated in the results of Sinha et al. [9].

Unsteady flow features are distinctly different between `NoTurb` and `01NWL1`. Laminar shear layer instabilities manifest across the coolant-hot gas shear layer when upstream turbulent fluctuations are absent. These flow features are not present when near-wall and 20% FST is introduced and the shear layer is turbulent. These two turbulent inflow cases show increased velocity fluctuations away from the jet centreline promoting lateral coolant spread while the turbulence conditions show contrasting states of turbulence anisotropy in the near-wall and coolant jet regions.

In the early stages of the coolant jet development, the high FST case (`20FSTL1`) shows an increased turbulent heat flux, quantifying the increased mixing capability of the flow. However, in the downstream region, the streamwise and normal components of turbulent heat flux reduced to below case `NoTurb` and `01NWL1`. Along the centreline, cases `NoTurb` and `01NWL1` show similar behaviour downstream, but contrasting behaviour is shown where the laminar instabilities are present in case `NoTurb`.

The impact of FST shows large integral length scales across the coolant jet that maintain a similar scale consistent with the upstream flow. At the coolant hole trailing edge, the near-wall length scales are driven by the smaller scale turbulent flow from the coolant hole for all three cases. Case `01NWL1` shows larger scales than `NoTurb`, with greater transverse length scales off the centreline, promoting the lateral mixing away from the coolant jet.

In summary, it is shown that inflow turbulence can have a strong impact on coolant distributions downstream as a consequence of the turbulent state of the coolant jet and the incoming flow. Hence, it is recommendable to always prescribe the inflow boundary conditions as accurately as possible in this regard. Turbulent boundary layer fluctuations are a key factor promoting lateral coolant spread. FST, which is commonly present in industrial applications and which can be highly variable, leads to drastically different coolant distribution across the cooled surface. While the latter can be highly problem-dependent, e.g. its integral scale and anisotropy, its impact on coolant mixing should be taken into account in simulations of film cooling flows.

Declaration of Competing Interest

None.

CRediT authorship contribution statement

C.D. Ellis: Conceptualization, Methodology, Software, Validation, Formal analysis, Investigation, Data curation, Writing – original draft, Writing – review & editing, Visualization. **H. Xia:** Conceptualization, Writing – review & editing, Supervision, Project administration, Funding acquisition.

References

[1] S. Acharya, D.H. Leedom, Large eddy simulations of discrete hole film cooling with plenum inflow orientation effects, J. Heat Transf. (2012).
[2] P. Renze, W. Schroder, M. Meinke, Large-eddy simulation of film cooling flows with variable density jets, Flow Turbul. Combust. 80 (2008) 119–132.
[3] J.E. Mayhew, J.W. Baughn, A.R. Byerley, The effect of freestream turbulence on film cooling adiabatic effectiveness, Int. J. Heat Fluid Fl. 24 (5) (2003) 669–679.
[4] A. Kohli, D.G. Bogard, Effects of very high free-stream turbulence on the jet-mainstream interaction in a film cooling flow, J. Turbomach. 120 (1998) 785–790.

[5] X. Chen, H. Xia, A hybrid LES-RANS validation of effusion cooling array measurements, in: 23rd ISABE Conference, 2017, pp. 1–15.
[6] M.L. Busche, J.E. Kingery, F.E. Ames, Slot film cooling in an accelerating boundary layer with high free-stream turbulence, Heat Transfer of Turbo Expo: Power for Land, Sea, and Air, Vol. 5B, 2014.
[7] Y. Kanani, S. Acharya, F. Ames, Simulations of slot film-cooling with freestream acceleration and turbulence, J. Turbomach. 140 (4) (2018).
[8] R.P. Schroeder, K.A. Thole, Effect of high freestream turbulence on flowfields of shaped film cooling holes, J. Turbomach. 138 (9) (2016).
[9] A.K. Sinha, D.G. Bogard, M.E. Crawford, Film-cooling effectiveness downstream of a single row of holes with variable density ratio, J. Turbomach. 113 (July) (1991) 442–449.
[10] J.R. Pietrzyk, D.G. Bogard, M.E. Crawford, Hydrodynamic measurements of jets in crossflow for gas turbine film cooling applications, J. Turbomach. 111 (1989) 139–145.
[11] OpenCFD Ltd 2017, OpenFOAM v17.12, 2017, (https://www.openfoam.com/releases/openfoam-v1712/).
[12] F. Nicoud, F. Ducros, Subgrid-scale stress modelling based on the square of the velocity gradient tensor, Flow Turbul. Combust. 62 (1999) 183–200.
[13] F. Duchaine, A. Corpron, L. Pons, V. Moureau, F. Nicoud, T. Poinsot, Development and assessment of a coupled strategy for conjugate heat transfer with large eddy simulation: application to a cooled turbine blade, Int. J. Heat Fluid Fl. 30 (6) (2009) 1129–1141.
[14] F. Duchaine, M. Boileau, Y. Sommerer, T. Poinsot, Large eddy simulation of flow and heat transfer around two square cylinders in a tandem arrangement, J. Heat Transf. 136 (10) (2014) 101702.
[15] S. Scholl, T. Verstraete, F. Duchaine, L. Gicquel, Conjugate heat transfer of a rib-roughened internal turbine blade cooling channel using large eddy simulation, Int. J. Heat Fluid Fl. 61 (2016) 650–664.
[16] A. Schindler, B.A. Younis, B. Weigand, Large-eddy simulations of turbulent flow through a heated square duct, Int. J. Therm. Sci. 135 (May 2018) (2019) 302–318.
[17] C.D. Ellis, H. Xia, Turbulent closure analysis in heated separated and reattached flow using eddy-resolving data, Phys. Fluids 32 (4) (2020) 045115.
[18] M. Klein, A. Sadiki, J. Janicka, A digital filter based generation of inflow data for spatially developing direct numerical or large eddy simulations, J. Comput. Phys. 186 (2) (2003) 652–665.
[19] M.C. Immer, Time-resolved measurement and simulation of local scale turbulent urban flow, ETH Zurich, 2016 Ph.D. thesis.
[20] S.B. Pope, Turbulent Flows, Cambridge University Press, 2000, doi:10.1017/CBO9780511840531.
[21] C. Bogey, O. Marsden, C. Bailly, Influence of the initial turbulence level on the flow and sound fields of a 10^5, J. Fluid Mech. 701 (2012) 352–385.
[22] S. Banerjee, R. Krahl, F. Durst, C. Zenger, Presentation of anisotropy properties of turbulence, invariants versus eigenvalue approaches, J. Turbomach. 8 (2007).